Optics Letters

Single-modulator, dual comb serrodyne spectroscopy

Jasper R. Stroud,[1,*] David A. Long,[2] and David F. Plusquellic[1]

[1]National Institute of Standards and Technology, Boulder, Colorado 80305, USA
[2]National Institute of Standards and Technology, Gaithersburg, Maryland 20899, USA
*jasper.stroud@nist.gov

Received 4 May 2024; revised 30 May 2024; accepted 30 May 2024; posted 31 May 2024; published 3 July 2024

Dual optical frequency comb spectroscopy allows for high speed, broadband measurements without any moving parts. Here, we combine differential chirp downconversion to probe large spectral bandwidths and serrodyne modulation to separate the positive and negative sidebands in a single modulator. As an initial demonstration, we apply this approach to measure a sharp cavity resonance to illustrate the system performance. We then measure methane transitions in the near-infrared and compare the resulting spectra to models based upon the current spectroscopic databases. The serrodyne method has lower hardware requirements compared to many existing approaches, and its simplicity enables a high degree of mutual coherence between the two combs. Further, this method is readily amenable to chip-scale photonic integration.

https://doi.org/10.1364/OL.529147

Dual optical frequency comb spectroscopy has proven to be an invaluable tool for applications ranging from hyperspectral imaging and high-speed sensing to trace gas detection [1]. Frequency combs generated by electro-optic (EO) modulators are often limited in bandwidth but take advantage of mutual phase coherence by generating both combs with a single laser [2–4]. These EO modulation techniques produce both positive and negative sidebands, generally requiring the addition of an acousto-optic modulator (AOM) to separate them in the downconversion process. We have previously demonstrated single frequency comb spectroscopy using serrodyne modulation with a single dual Mach–Zehnder phase modulator to achieve the same sideband separation effect without an AOM [5]. This single element design significantly reduces the system's complexity and enables its integration because of the incompatibility of AOM materials in integrated photonic platforms. Here, we advance this technique by extending it to dual comb spectroscopy using a differential chirped pulse downconversion method [6–8], allowing us to sample wide bandwidths at high speed and resolutions spanning over three orders of magnitude.

While a few other approaches for dual comb spectroscopy with a single modulator have been demonstrated, these techniques generally filter either the positive or negative sidebands to remove the degeneracy in the radio frequency (RF) domain. This reduces the comb bandwidth by a factor of two [9] and adds hardware complexity to the system after the sample [10].

We have previously reported on a differential chirp downconversion scheme that uses one chirped pulse to probe a system (SIG) and another chirped pulse acting as a local oscillator (LO) to downconvert the information into the RF domain (see Supplement 1). We acquire both time and frequency domain spectra, where the frequency domain spectrum is temporally magnified compared to the time domain spectrum with a magnification factor defined as

$$m = \frac{\Delta f_{\mathrm{SIG}}}{\Delta f_{\mathrm{LO}} - \Delta f_{\mathrm{SIG}}}, \tag{1}$$

where Δf_{SIG} and Δf_{LO} are the bandwidths of the SIG chirp and LO chirp, respectively. The bandwidth of the downconverted RF signal is defined as the difference between the SIG and LO chirps,

$$\Delta f_{\mathrm{RF}} = \Delta f_{\mathrm{LO}} - \Delta f_{\mathrm{SIG}}. \tag{2}$$

The chirp rate of the SIG chirp is defined as

$$\alpha_{\mathrm{SIG}} = \frac{\Delta f_{\mathrm{SIG}}}{\tau_{\mathrm{CP}}} \tag{3}$$

where τ_{CP} is the duration of the chirped pulse. This chirp rate defines the time and frequency relation. If the chirp rate or magnification factor is large enough, we see rapid passage effects in the frequency domain and possibly in the time domain [8]. The spectral resolution of this technique is defined by the SIG chirp rate and RF chirp bandwidth:

$$\delta_{\mathrm{SIG}} = \frac{\Delta f_{\mathrm{SIG}}}{\Delta f_{\mathrm{RF}} \tau_{\mathrm{CP}}} = \frac{\alpha_{\mathrm{SIG}}}{\Delta f_{\mathrm{RF}}}. \tag{4}$$

In this demonstration, both the traditional SIG and LO chirped pulses are generated by the same modulator, and both pass through the system under test. Unlike the previous work, the SIG and LO chirps are functionally indistinguishable, both acting as probes of the system and as respective local oscillators at the detector. This also means that the chirp rate of the SIG and chirp rate of the LO defines different system resolution and bandwidth:

$$\delta_{\mathrm{LO}} = \frac{\alpha_{\mathrm{LO}}}{\Delta f_{\mathrm{RF}}}, \tag{5}$$

where α_{LO} is the chirp rate of the LO. The system here has two different time and frequency axis relations, and therefore two different optical resolutions and bandwidths. If this difference is large, two copies of the spectra can be resolved. By decreasing these differences, the two spectra can nearly overlap, mitigating

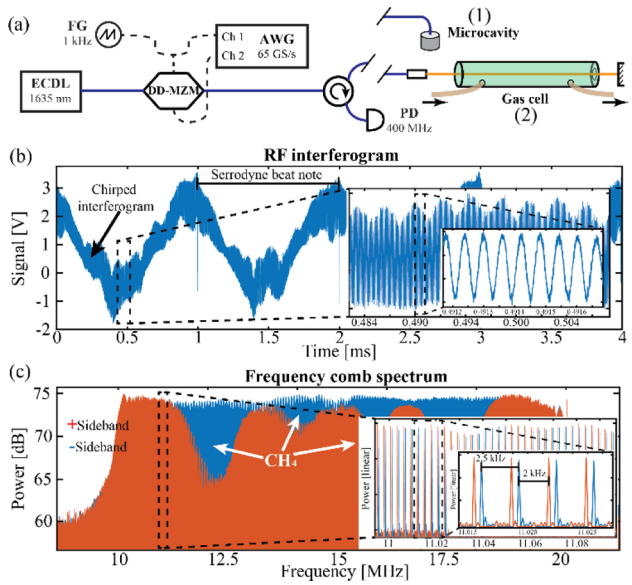

Fig. 1. (a) System diagram for (1) microcavity probe and (2) spectroscopy of methane at 1635 nm. Abbreviations: EDCL, external cavity diode laser; DD-MZM, dual-drive Mach–Zehnder modulator; FG, function generator; AWG, arbitrary waveform generator; PD, photodetector. (b) Sampled RF interferogram showing the 1 kHz serrodyne modulation, and the insets show the magnified chirped interferogram. (c) Fourier transform of the repeated interferogram in (b) to show the comb spectrum with lines spanning from 10 to 20 MHz. The positive sideband is colored in red and negative sideband in blue, with the CH_4 absorption features detailed in Fig. 5(a) seen in red. The inset shows the comb on a linear intensity scale.

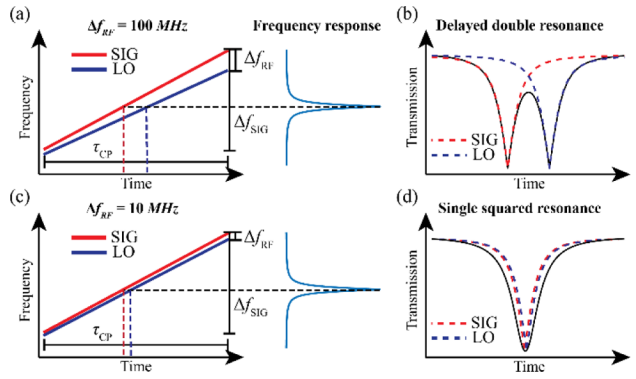

Fig. 2. (a) Model spectrogram is shown with the SIG in red and LO in blue where their different slopes interact with the resonance at different times. (b) Individual (dashed) and combined (solid) model spectra defined by a 100 to 200 MHz RF span. (c) Corresponding spectrogram with a smaller 10 to 20 MHz RF bandwidth, and (d) nearly overlapped individual (dashed) and combined (solid) spectra.

any decrease in the resolution caused by this overlap. In this work, we demonstrate two cases for the differential chirp down-conversion and apply the technique to an optical microcavity resonance and the near-infrared spectroscopy of methane. By incorporating all of the optical modulation into a single EO element, we reduce the optical propagation losses and enable this method for an integrated platform.

Figure 1(a) shows the simple hardware implementation, using an external cavity diode laser (ECDL) at 1635 nm sent into a single dual-drive Mach–Zehnder modulator (DD-MZM). The DD-MZM is driven by an arbitrary waveform generator (AWG) that defines the chirps and a function generator (FG) that defines the serrodyne modulation (set for a 1 kHz modulation). The serrodyne modulation is defined as a sawtooth waveform with an amplitude corresponding to a 2π phase shift [5]. Due to the differential relationship between the frequency and phase, $f = d\varphi/dt$, the linear phase modulation shifts the frequency of the input laser [11,12]. While the AWG could perform the serrodyne modulation in addition to the chirp, using the FG was practical and we plan to replace the AWG with simpler hardware [5].

The modulator output is sent into a microcavity or evacuable gas cell and then to a photodetector (PD). The SIG and LO chirps that have both interacted with the sample mix at the detector to yield a RF interferogram. The SIG chirp spans a $f_{start} = 1$ GHz to $f_{stop} = 11$ GHz chirp bandwidth that generates a total span of 22 GHz in the EOM's first order [6]. The LO chirp spans from $f_{start} - f_{RFstart}$ to $f_{stop} - f_{RFstop}$, and both have a $\tau_{CP} = 400\,\mu$s chirp duration. The chirps are repeated for $N_{chirps} = 10$ times to form a 4 ms record in the RF domain that Fourier transforms into a comb that spans from $f_{RFstart}$ to f_{RFstop}. Here we show results using a RF span from 100 to 200 MHz and from 10 to 20 MHz.

A typical RF interferogram is shown in Fig. 1(b), where the 1 kHz serrodyne modulation is evident over the 4 ms waveform record. The inset in Fig. 1(b) shows the zoomed-in section of the interferogram, revealing part of the repeated chirped waveform. The Fourier transform of Fig. 1(b) is shown in Fig. 1(c) which spans from 10 to 20 MHz and consists of two interleaved combs with 4000 lines in each sideband. The interleaved positive and negative sideband comb lines have been highlighted in red and blue, respectively, to illustrate the four methane absorption lines on the positive half. The insets in Fig. 1(c) show i) the separation of the two sideband combs by twice the 1 kHz serrodyne frequency and ii) the comb tooth spacing of 2.5 kHz that is inversely related to the 400 µs chirp duration. The time domain interferogram has a signal-to-noise ratio (SNR) of approximately 15 dB in the inset in Fig. 1(b), while the comb tooth SNR varies between 13 and 16 dB as evident in Fig. 1(c).

These two cases are illustrated in Fig. 2 where the device under test is an optical microcavity with a length of L = 206 µm and mirror reflectivities of $R = 0.9994$, resulting in cavity resonances with full-width at half-maxima (FWHM) near 80 MHz (see Ref. [13] for further details on the microcavity and its fabrication). The case where the RF comb spans from 100 to 200 MHz is shown in Fig. 2(a), where the SIG chirp in red and LO chirp in blue both interact with the frequency response of the system. Because the chirp rates (slopes in Figs. 2(a) and 2(c)) of the SIG and LO are different, they interact with the resonance dip at different times. This results in the spectra shown in Fig. 2(b), where there are two distinct resonances largely separated in time. By decreasing the span of the RF comb, the times at which the SIG and LO pass through the resonance are nearly the same. Figure 2(c) shows how a RF span from 10 to 20 MHz reduces the separation between the two resonances and results in the nearly single resonance of the squared magnitude illustrated in Fig. 2(d). The optical resolution is an order of magnitude coarser because of its inverse relationship with the RF bandwidth.

We show the experimental results from the microcavity for an RF comb spanning 100 to 200 MHz in Fig. 3. The double resonance dip is seen in both the time and frequency domain data. Because the RF spans from 100 to 200 MHz, the separation

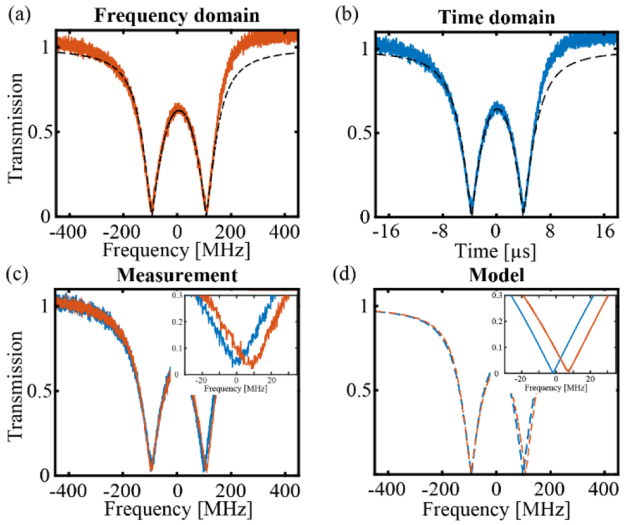

Fig. 3. (a) Frequency domain in red and (b) time domain spectra in blue and model in dashed black. (c) The time and frequency spectra overlapped with the small offset shown in the inset. (d) Corresponding model showing the same offset on the right mostly dip in red.

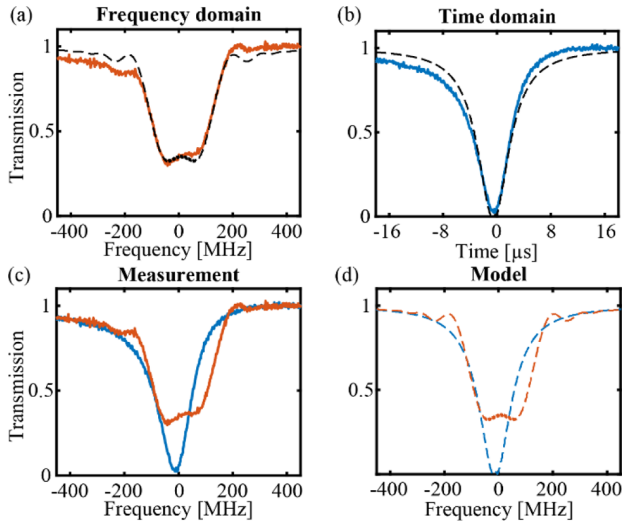

Fig. 4. (a) Frequency domain spectra in red showing magnified rapid passage effects in both directions and (b) unmagnified time domain spectra in blue and model in dashed black. (c) Time and frequency spectra overlayed and (d) corresponding models.

between the two dips also changes depending on where it appears in the spectrum. The model (black) overlaid in Fig. 3(a) was frequency shifted by ≈190 MHz to match the experimental data (red). The SIG magnification factor defined in Eq. (1) is 100 for the 10 GHz SIG bandwidth and the 100 MHz RF bandwidth. Because of the slow chirp rate of the SIG (25 kHz/μs), we do not see any rapid passage effects in either spectrum [14].

The cavity resonance model is

$$H(\omega) = \frac{(1-R)exp(i\pi f\tau)}{(1-Rexp(i2\pi f\tau))}, \tag{6}$$

where $H(\omega)$ is the frequency response of the cavity and $\tau = 2nL/c$, with n being the refractive index of air and c is the speed of light [15]. The transfer function in Eq. (6) mixes with the SIG and LO chirps and then are convolved with the LO and SIG chirps, respectively, to give

$$I(\omega) = C_{LO}(\omega) * (C_{SIG}(\omega)H(\omega)) + C_{SIG}(\omega) * (C_{LO}(\omega)H(\omega)) \tag{7}$$

where $C(\omega)$, is the frequency domain representation of the SIG and LO chirp functions. The frequency and time domain models are given by $I(\omega)$ and the inverse Fourier transform, $F^{-1}\{I(\omega)\}$, respectively. Figure 3(a) shows the frequency domain data in red and model in black, and Fig. 3(b) shows the corresponding time domain data and model.

The time and frequency data are shown in Fig. 3(c), where we see nearly identical spectra except for a small offset on the right most dip (red) that corresponds to the LO chirp. Here, we choose to correlate the time and frequency domains using the SIG chirp rate, meaning the resonance dip corresponding to the SIG chirp will match up in both time and frequency domains, and consequently the LO resonance dip will be offset. The model in Fig. 3(d) shows the same offset of approximately 9 MHz. The optical resolution of the SIG is defined by Eq. (4) as 250 kHz, while the LO resolution is 247.5 kHz. Because both are much smaller than the 100 to 200 MHz frequency offset, the distinct double dip shown in Fig. 3 is expected. Since these features are well separated, phase information also can be recovered (the corresponding phase spectra are shown in the Supplement 1).

The RF comb bandwidth is then reduced to span 10 to 20 MHz, making the difference between the SIG and LO chirps tenfold smaller. Consequently, the SIG magnification factor is increased tenfold to 1000 with the 10 GHz chirp and 10 MHz RF bandwidth. Because of the tenfold fewer comb teeth in Fig. 4, the SNR per comb tooth is higher in Fig. 4 than in Fig. 3. At the same chirp rate of 25 kHz/μs, the magnified frequency domain chirp rate is now well above the ≈1 MHz/μs threshold to see rapid passage effects. Figure 4(a) shows the frequency domain data in red and model in black, where there are distinct ripples going in both directions due to rapid passage effects. The magnification from the LO (the first term in Eq. (7)) generates ripples in one direction while the SIG magnification (the second term in Eq. (7)) generates ripples in the opposite direction. Because the LO chirp spans slightly less bandwidth, the corresponding magnification factor will also be slightly less than the SIG magnification factor. This gives the spectra and model shown in Fig. 4(a), while in Fig. 4(b), the time domain data and model show an unmagnified resonance line shape with a squared magnitude. When we compare the time and frequency domain data in Fig. 4(c), we see a background asymmetry they both share, i.e., a lower background level on the higher frequency side. While our model in Fig. 4(d) does not reflect this background asymmetry, this effect has been previously reported and modeled using a Fano resonance line shape [8].

We then utilize the 10 MHz RF bandwidth system to probe methane in a 1 m double passed evacuable cell shown in Figure 2(a). Pure methane spectra are ratioed against those from an evacuated cell, while N_2-broadened methane measurements are in reference to pure N_2 at the same pressure. First, the gas cell is filled with methane to 1.38 kPa (10.4 Torr) and the ECDL center frequency was set to 6114.5845 cm^{-1} to measure the R10 manifold containing four unresolved features over a 10 GHz single sideband bandwidth. We use the 2008, 2016, and 2020 HITRAN databases [16–18] to fit the methane spectra. Figure 5(a) shows the experimental time domain spectra in blue. For the pure sample, we find the best fit spectra are from the most recent HITRAN

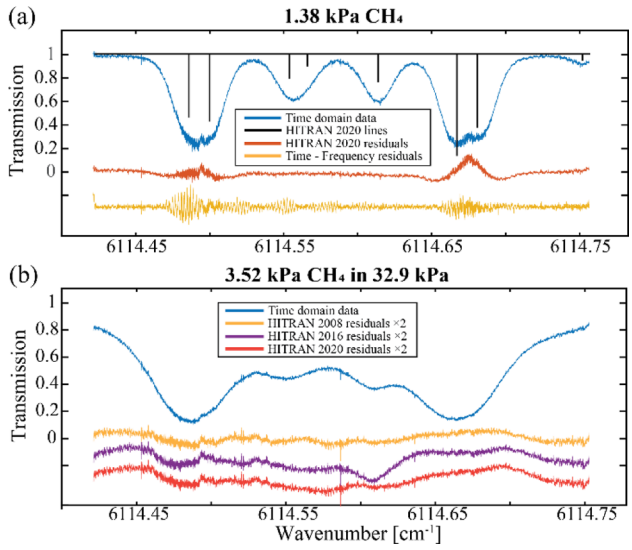

Fig. 5. (a) Measured methane spectra at 1.38 kPa (10.4 Torr) (blue trace) are best fit using the HITRAN 2020 spectroscopic parameters, with the residuals shown in red. The difference between the time and frequency domain residuals is shown in yellow to illustrate rapid passage effects. (b) Measured methane spectra for 3.52 kPa (26.4 Torr) methane in 32.9 kPa (247 Torr) total pressure (blue) is best fit using the HITRAN 2008 database (residuals in yellow).

2020 database with the residuals shown in red. We see some potential saturation of the first and last line pair showing up as nearly symmetric residuals. The line locations are shown above in black. The sharp feature in the first line pair manifests as high frequency ripples in the frequency domain residuals shown in yellow.

We then fill the cell with 3.52 kPa (26.4 Torr) of methane and backfill with N_2 up to 32.9 kPa (247 Torr) to pressure broaden the four lines such that they overlap significantly. The increased collisional deactivation significantly reduces any rapid passage effects. Figure 5(b) shows the pressure broadened methane spectra in blue where now the best fit model is to the HITRAN 2008 database (residuals shown in yellow). In contrast to the results in Fig. 5(a), the frequency domain spectrum (not shown) is nearly identical to that shown in the time domain. Both the HITRAN 2020 and HITRAN 2016 databases result in similar residuals shown in red and purple, respectively. These results indicate the spectroscopic parameters have improved for pure methane but have gotten worse for pressure broadened spectra that are needed for atmospheric sensing of this important greenhouse gas [19].

In summary, a dual-comb chirped-pulse serrodyne method based a single dual Mach–Zehnder phase modulator is discussed for performing high resolution spectroscopy where both the SIG and LO chirps sequentially interrogate the sample. For a sharp resonance of a microcavity, a lower magnified response can give a resolved doubled spectrum shown in Fig. 3, while a highly magnified response can lead to the double-sided rapid passage line shapes shown in Fig. 4. We show how the chirp parameters that define the RF bandwidth control the magnification and therefore the spectral separation and resolution under a variety of sample conditions. The chosen parameters depend on the sensing requirements of the system; for example, sensing the motion of the cavity resonance only requires the center frequency [8], and fitting GHz wide molecular features with kHz to MHz resolution is key for room temperature Doppler-broadened to Doppler-free spectroscopy [20]. The larger RF bandwidth design has finer resolution than the smaller RF bandwidth system and therefore gives improved accuracy of the resonance dip locations or spectral fingerprint. Additionally, phase information that is normally lost in the SIG + LO configuration can be recovered.

The approach discussed here for performing dual comb spectroscopy using a single modulator significantly reduces the overall hardware complexity of the system. To demonstrate the versatility of the system, we perform measurements over a microcavity resonance, with a FWHM of less than 100 MHz and with features close to our MHz level system resolution, to illustrate the concepts and trade-offs. We then apply the method to measure the R10 manifold of CH_4, showing GHz wide features over 10 GHz of the optical bandwidth. These results provide a clear pathway for integrated photonic applications that enable differential chirp dual comb sensing and spectroscopy where acousto-optic modulators cannot be readily integrated. Current efforts are under way to extend this technique to higher EO orders [6] to sample over larger absorption bandwidths.

Acknowledgment. We acknowledge helpful discussions with K. A. Briggman, B. J. Reschovsky, and N. A. Malarich.

Disclosures. The authors have no conflicts of interest to disclose.

Data availability. Data underlying the results presented in this paper are available in Ref. [21].

Supplemental document. See Supplement 1 for supporting content.

REFERENCES

1. R. Liao, H. Tian, W. Liu, *et al.*, JPhys Photonics **2**, 042006 (2020).
2. A. Parriaux, K. Hammani, and G. Millot, Adv. Opt. Photonics **12**, 223 (2020).
3. D. A. Long, A. J. Fleisher, K. O. Douglass, *et al.*, Opt. Lett. **39**, 2688 (2014).
4. P. Martin-Mateos, M. Ruiz-Llata, J. Posada-Roman, *et al.*, IEEE Photonics Technol. Lett. **27**, 1309 (2015).
5. D. A. Long, S. M. Bresler, Y. Bao, *et al.*, Opt. Lett. **48**, 892 (2023).
6. J. R. Stroud, J. B. Simon, G. A. Wagner, *et al.*, Opt. Express **29**, 33155 (2021).
7. J. R. Stroud and D. F. Plusquellic, Opt. Lett. **47**, 3716 (2022).
8. D. A. Long, J. R. Stroud, B. J. Reschovsky, *et al.*, APL Photonics **8**, 091302 (2023).
9. M. Soriano-Amat, M. A. Soto, V. Duran, *et al.*, J. Lightwave Technol. **38**, 5107 (2020).
10. J. H. Huh, Z. Chen, E. Vicentini, *et al.*, Opt. Lett. **46**, 3957 (2021).
11. L. M. Johnson and C. H. Cox, J. Lightwave Technol. **6**, 109 (1988).
12. I. Y. Poberezhskiy, B. Bortnik, J. Chou, *et al.*, IEEE J. Quantum Electron. **41**, 1533 (2005).
13. F. Zhou, Y. Bao, R. Madugani, *et al.*, Optica **8**, 350 (2021).
14. M. J. Lawrence, B. Willke, M. E. Husman, *et al.*, J. Opt. Soc. Am. B **16**, 523 (1999).
15. Y. Xiao, D. N. Maywar, and G. P. Agrawal, J. Opt. Soc. Am. B **28**, 1685 (2011).
16. L. S. Rothman, I. E. Gordon, A. Barbe, *et al.*, J. Quant. Spectrosc. Radiat. Transfer **110**, 533 (2009).
17. I. E. Gordon, L. S. Rothman, C. Hill, *et al.*, J. Quant. Spectrosc. Radiat. Transfer **203**, 3 (2017).
18. I. E. Gordon, L. S. Rothman, R. J. Hargreaves, *et al.*, J. Quant. Spectrosc. Radiat. Transfer **277**, 107949 (2022).
19. J. R. Stroud, G. A. Wagner, and D. F. Plusquellic, Remote Sens. **15**, 5595 (2023).
20. X. Ren, J. Pan, M. Yan, *et al.*, Nat. Commun. **14**, 5037 (2023).
21. J. R. Stroud, D. A. Long, and D. F. Plusquellic, "Single-modulator, dual comb serrodyne spectroscopy," MDS (2024), https://doi.org/10.18434/mds2-3246.